DETECTING NANOFLARE HEATING EVENTS IN SUBARCSECOND INTER-MOSS LOOPS USING Hi-C

AMY R. WINEBARGER[1], ROBERT W. WALSH[2], RONALD MOORE[1], BART DE PONTIEU[3], VIGGO HANSTEEN[4], JONATHAN CIRTAIN[1],
LEON GOLUB[5], KEN KOBAYASHI[6], KELLY KORRECK[5], CRAIG DEFOREST[7], MARK WEBER[5], ALAN TITLE[3], AND SERGEY KUZIN[8]
[1] NASA Marshall Space Flight Center, ZP 13, Huntsville, AL 35812, USA; amy.r.winebarger@nasa.gov
[2] University of Central Lancashire, Preston, Lancashire PR1 2HE, UK
[3] Lockheed Martin Solar and Astrophysics Lab, 3251 Hanover St., Org. A0215, Bldg. 252, Palo Alto, CA 94304, USA
[4] Institute of Theoretical Astrophysics, University of Oslo, P.O. Box 1029 Blindern, N-0315 Oslo, Norway
[5] Harvard-Smithsonian Center for Astrophysics, 60 Garden St., Cambridge, MA 02138, USA
[6] Center for Space Plasma and Aeronomic Research, The University of Alabama in Huntsville, 320 Sparkman Dr, Huntsville, AL 35805, USA
[7] Southwest Research Institute, 1050 Walnut Street, Suite 300, Boulder, CO 80302, USA
[8] P.N. Lebedev Physical institute of the Russian Academy of Sciences, Leninskii prospekt 53 119991, Moscow

ABSTRACT

The High-resolution Coronal Imager (Hi-C) flew aboard a NASA sounding rocket on 2012 July 11 and captured roughly 345 s of high-spatial and temporal resolution images of the solar corona in a narrowband 193 Å channel. In this paper, we analyze a set of rapidly evolving loops that appear in an inter-moss region. We select six loops that both appear in and fade out of the Hi-C images during the short flight. From the Hi-C data, we determine the size and lifetimes of the loops and characterize whether these loops appear simultaneously along their length or first appear at one footpoint before appearing at the other. Using co-aligned, co-temporal data from multiple channels of the Atmospheric Imaging Assembly on the *Solar Dynamics Observatory*, we determine the temperature and density of the loops. We find the loops consist of cool ($\sim 10^5$ K), dense ($\sim 10^{10}$ cm^{-3}) plasma. Their required thermal energy and their observed evolution suggest they result from impulsive heating similar in magnitude to nanoflares. Comparisons with advanced numerical simulations indicate that such dense, cold and short-lived loops are a natural consequence of impulsive magnetic energy release by reconnection of braided magnetic field at low heights in the solar atmosphere.

Key word: Sun: corona

Online-only material: animation

1. INTRODUCTION

Since the advent of X-ray and EUV space borne imagers, scientists have been studying "coronal loops" or the one-dimensional structures formed in the solar corona by hot plasma flowing along magnetic field lines. The majority of loop studies in active regions have focused on two types of loops: EUV loops and active region core loops (e.g., Reale 2010). The early observational characteristics of EUV loops found the loops did not agree with the temperature and density stratification predicted by steady heating hydrodynamic models (e.g., Lenz et al. 1999a; Aschwanden et al. 2000; Lenz et al. 1999b; Winebarger et al. 2003). A study of the evolution of these loops found that they were evolving with time and appeared in channels sensitive to higher temperature plasma before appearing in cooler temperature channels (Winebarger et al. 2003; Mulu-Moore et al. 2013). Almost immediately it was suggested that these loops were the results of a short burst of impulsive heating events occurring on many sub-resolution strands because their extended decay times do not match those of single strand events (Warren et al. 2002, 2003); this heating scenario is now commonly called a "short nanoflare storm" (Klimchuk 2006).

The active region core loops are typically shorter, high temperature (>2 MK) loops that are found in regions of strong magnetic field in an active region. The footpoints of these hot loops form a reticulated pattern in EUV images, called "moss" (e.g., Fletcher & de Pontieu 1999; Berger et al. 1999; De Pontieu et al. 2013). Unlike EUV loops, which are observed to evolve and cool, the core loops and moss are relatively steady over many hours of observations (Antiochos et al. 2003;

Warren et al. 2010, 2011; however, see Viall & Klimchuk 2012). Klimchuk (2009) has suggested these loops can be explained by a so-called long nanoflare storm. In this scenario, the core is made up of many sub-resolution strands. The strands are heated impulsively and infrequently, so the plasma along each strand will likely cool to background temperatures before being re-heated. There have been multiple studies of the expected observational consequences of this heating scenario using one-dimensional hydrodynamic codes (e.g., Patsourakos & Klimchuk 2005; Sarkar & Walsh 2008, 2009; Bradshaw et al. 2012). One prediction of this scenario is that the cooling strands should appear in the inter-moss regions.

In this paper, we present an analysis of subarcsecond loops observed with the High-resolution Coronal Imager (Hi-C), which has obtained high-spatial and temporal resolution images of the solar corona during a sounding rocket flight. We identify six loops that appear in the inter-moss region of the active region core. These loops appear in and fade out of the Hi-C images within the 3.5 minutes of observations. With the Hi-C data, we characterize the loop length, width, and lifetime. Using co-aligned and co-temporal multiple channel images from the Atmospheric Imaging Assembly (AIA) on the *Solar Dynamics Observatory* (*SDO*), we also determine the loops' likely evolution, temperature, and density. We find that these loops never achieve million-degree temperatures. Instead they are cool ($\sim 10^5$ K), dense ($\sim 10^{10}$ cm^{-3}) loops that likely originate from small-scale reconnection events. The required thermal energy and the observed evolution suggest that the loops are the result of impulsive energy release low in the solar atmosphere. The magnitude of the energy release is similar to that of the canonical nanoflare (Parker 1988), though in these
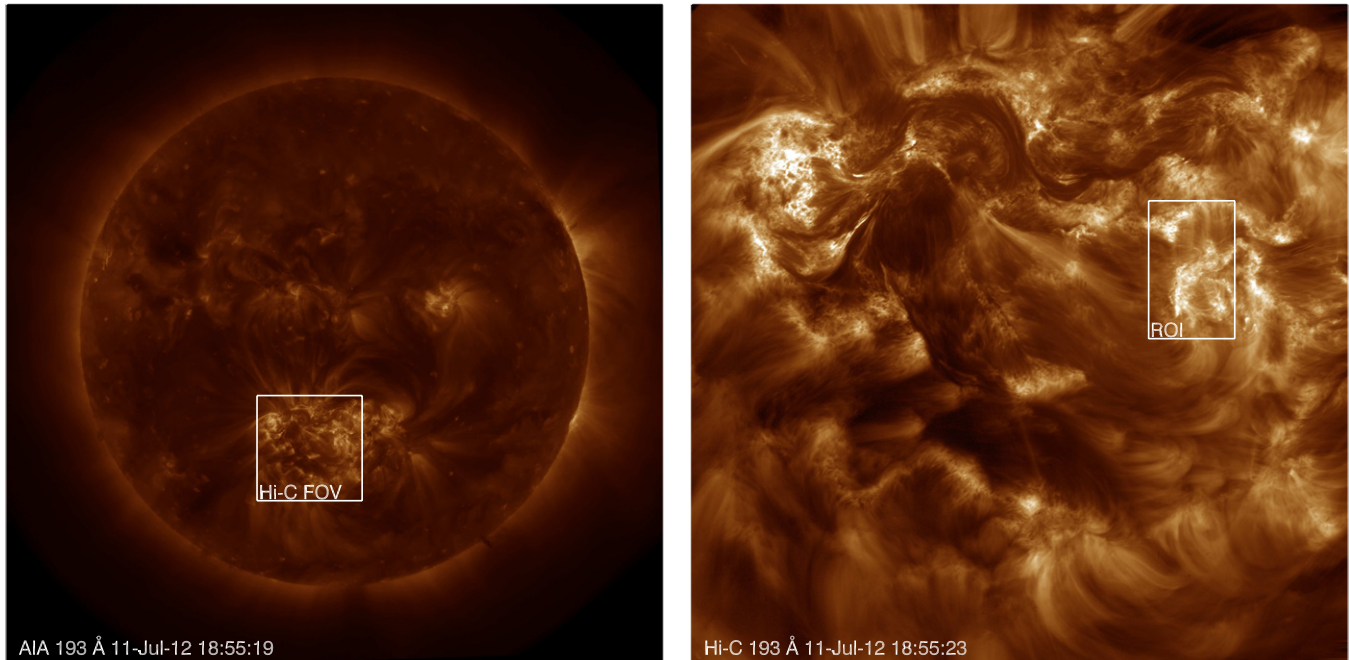
Figure 1. Left panel: AIA 193 Å full disk image with Hi-C FOV marked. Right panel: Hi-C image with the ROI marked.

loops the temperature of the plasma never reaches millions of degrees. Comparisons with advanced numerical simulations show that such loops occur naturally as the result of energy release at low heights by reconnection of braided magnetic field lines. The low heights and corresponding high densities result in strong radiative cooling which explains the short duration of these loops in the Hi-C images.

2. DATA AND ANALYSIS

The Hi-C telescope and rocket flight are described in detail by Kobayashi et al. (2013) and Cirtain et al. (2013). Hi-C is a Ritchey–Chretien telescope with a 220 mm diameter primary mirror. The primary and secondary mirrors have a multilayer coating that reflects only a narrow wavelength window around 193 Å. Entrance and focal plane filters are used to reduce the out-of-band light contamination. Hi-C is similar in wavelength response to that of the AIA 193 Å channel, but its effective area is 5.3 times larger in magnitude. Images are projected onto a 4096 × 4096 back-illuminated CCD. The plate scale of the images is $0\farcs1$ pixel^{-1}; the field of view (FOV) of the telescope is $6\farcs8 \times 6\farcs8$. The payload was launched at approximately 18:50 UT 2012 July 11 from White Sands Missile Range. Hi-C acquired 37 full-frame images from 18:52:49 to 18:56:10 with a 2 s exposure time (5.5 s cadence). The resolution of the images is a result of the point-spread function of the optics and the stability of the pointing control of the rocket. The initial seven frames were blurred due to rocket jitter. We estimate the remaining 30 images have a resolution of $0\farcs3$–$0\farcs4$. After the initial 37 full-frame images, Hi-C then obtained 86 partial frame images before the shutter door was closed. We only consider the full-frame images in this analysis.

The Hi-C data are dark-current subtracted and flatfielded to remove the shadow of the filter mesh on the images. The images are also corrected for atmospheric absorption by normalizing each image to the maximum of the total intensity summed over the image. There was a small drift of the telescope over the rocket flight, plus a re-point approximately 2.5 minutes

into data acquisition. This drift and re-point allow for the correction of dust particles on the detector. Using the aligned data cube, we replaced the values in the dust particles with the intensity measured at that same solar location at the closest time that was not affected by dust. The AIA (Lemen et al. 2012) and the Helioseismic Magnetic Imager (HMI) flown on the *SDO* recorded full-disk solar images and magnetic field measurements during the Hi-C rocket flight. The AIA data considered in this analysis includes six of the EUV/UV channels (94, 211, 193, 171, 304, and 1600 Å). Images in these channels were taken with a cadence of roughly 12 s. The pixel size of the AIA instrument is $0\farcs6$ pixel^{-1}; it has a spatial resolution of $\sim 1\farcs2$. *Hinode*'s X-Ray Telescope (XRT; Golub et al. 2007) was recording partial disk images using the Ti-poly filter; the FOV of the XRT overlapped the Hi-C FOV and included the region of interest (ROI) of this paper. The data were taken with long and short exposure times, which were then combined to single images. The AIA data were aligned to the Hi-C data by cross-correlating the AIA 193 Å image to the Hi-C 193 Å images. The AIA data were then aligned to the XRT data by cross-correlating the 94 Å images to the XRT images. The AIA and HMI data were aligned using aia_prep, though there is jitter in the AIA movies due to the heater being on during the flight.

The target of the Hi-C flight was Active Region 11520 centered at approximately $[-150, -281]$ arcsec from Sun center. The left panel of Figure 1 shows the full-disk AIA 193 Å image with the Hi-C FOV marked. The right panel shows the Hi-C FOV approximately 3.5 minutes into data acquisition (after the re-point). The FOV shown with the box is the ROI for this paper.

In Figure 2, we show the evolution of the ROI for this analysis in the Hi-C 193 Å channel. We first estimate the background intensity in this region as the minimum intensity in each pixel location over the 3.5 minutes of data; this background (minimum intensity) image is shown in the upper left panel of Figure 2. The remaining images show the background-subtracted Hi-C data at different times. The structures that have roughly steady intensity over the 3.5 minutes has been subtracted from these images, while dynamic evolving structures remain. The final
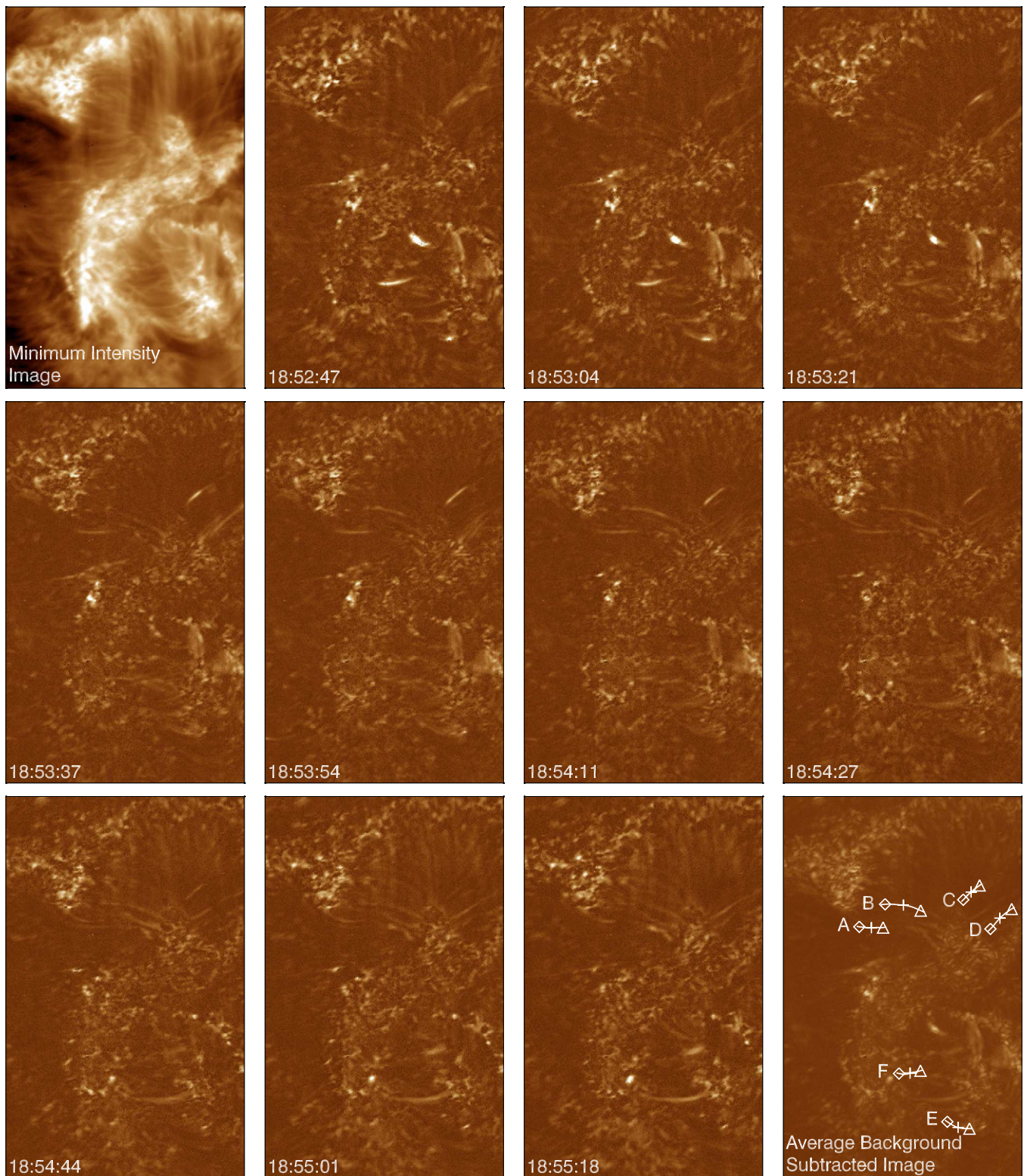
Figure 2. The top left panel shows the "minimum image" background that was subtracted from every subsequent image. The following frames show the background-subtracted images at a ∼20 s cadence. The final frame is the average of all background-subtracted images. Several loops are traced in the final image. Their eastern point, center point, and western point are shown with a diamond, plus sign and triangle, respectively.

frame in Figure 2 (lower right) shows the average of all the background-subtracted images.

We have identified several loops that appear and disappear during the 3.5 minutes of full-frame Hi-C data. These loops, labeled A–F, are shown in the last frame of Figure 2. These loops occur in inter-moss regions. Loops A–D do not appear to join the regions of moss, though this instrument may not image their footpoints. Loops E and F may join the regions of the moss.

Figure 3 shows the ROI in the XRT Ti-poly filter, the AIA 94, 211, 193, 171, 304, and 1600 Å channels, the Hi-C 193 Å channel and the HMI B_{los} measurements. In addition, a background-subtracted Hi-C 193 Å image is shown and the
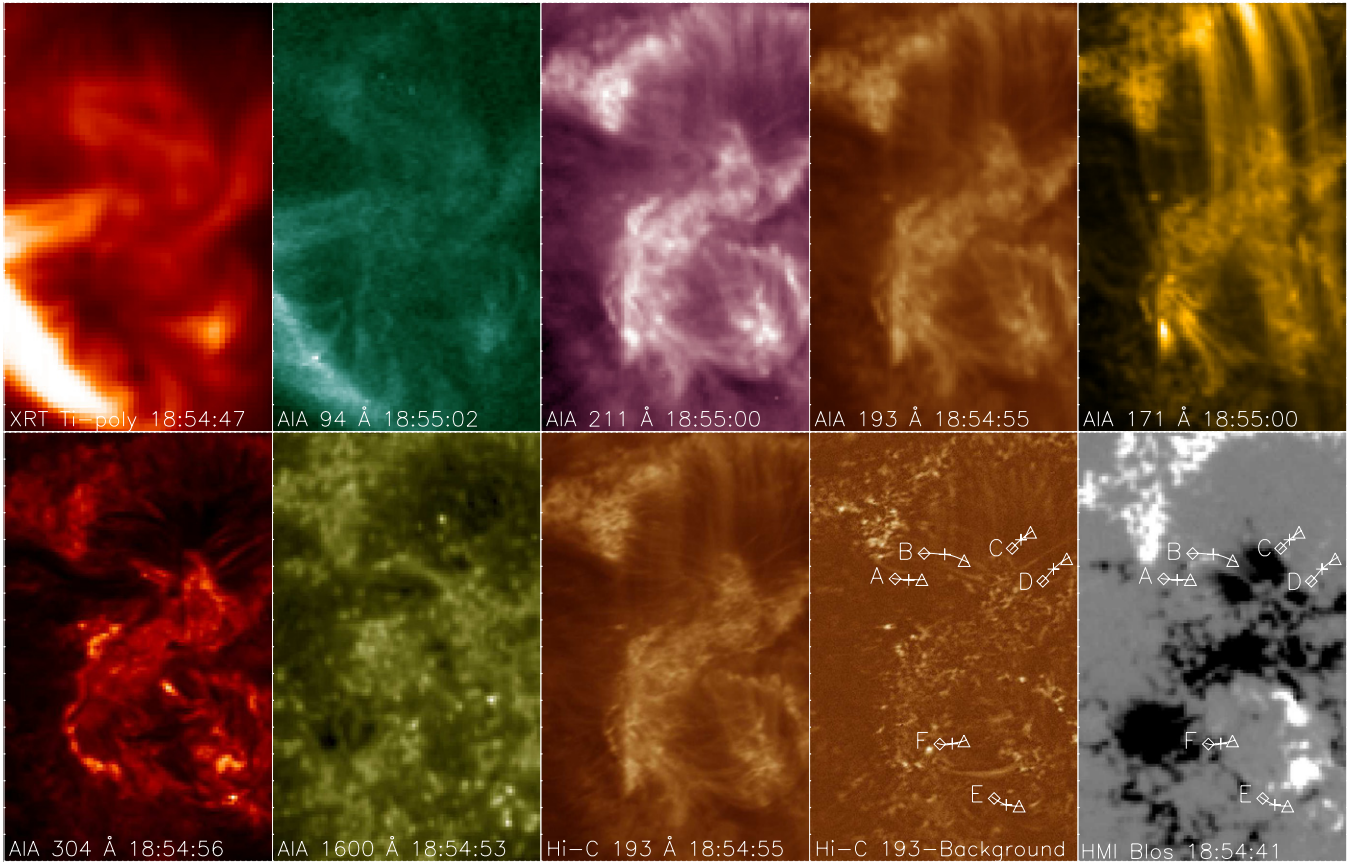
Figure 3. The region of interest for this analysis in the XRT Ti-poly filter, the AIA 94, 335, 211, 193, 171, 304, and 1600 Å channels, the Hi-C 193 Å channel, the background subtracted Hi-C 193 Å channel, and the HMI B_{los}.

(An animation of this figure is available in the online journal.)

loops are plotted on the background subtracted image and the magnetogram. Movies of this region (see on-line version) show the short-lived loops appearing and disappearing in the 3.5 minutes of Hi-C data. These loops are also observed in the lower-cadence AIA 171, 193, 211, and 304 Å images. Loop C is also apparent in the 1600 Å images. These loops do not appear in the AIA 94 Å or the XRT Ti-poly images.

2.1. Loop Evolution, Lifetime, Velocity, and Size

Figure 4 shows the normalized lightcurves of the loops in Hi-C 193 Å and AIA 304, 171, 193, and 211 Å channels. All lightcurves are the average intensity in ∼2 × 2 AIA pixels (11 × 11 Hi-C pixels) as a function of time, one centered about 10% from the eastern end of the loop (left column), one centered at the center of the loop (middle column), and one centered about 10% from the western end of the loop (right column). These three locations of the measured lightcurves are shown in the last panel of Figure 2 as a diamond, a plus sign, and a triangle, respectively. The peak of the Hi-C lightcurve (black line) is shown as a vertical dashed line in each panel; the time of the peak is given in each panel.

Though the light curves are noisy, they demonstrate that, at any location along the loop, the loop "appears" in all passbands nearly simultaneously. There is no indication that the loops appear in hotter passbands (like 211 Å shown in pink) before the cooler ones (like 171 Å shown in red); hence the loops do not appear to be cooling from coronal temperatures. Most, but not all, of the loops also appear in the 304 Å filter. The

Table 1
Loop Lifetimes, Velocities, and Diameters

Loop	Lifetime (s)	Velocity (km s^{-1})	Projected Length (km)	Width (km)
A	72.3 ± 5.5	NA	5000	704 ± 8
B	72.3 ± 5.5	180 ± 40	7500	675 ± 8
C	55.7 ± 5.5	−90 ± 10	4800	728 ± 8
D	77.9 ± 5.5	−290 ± 140	6100	782 ± 9
E	66.8 ± 5.5	−240 ± 120	4800	803 ± 14
F	39.0 ± 5.5	NA	4700	726 ± 8

absence of some of the loops could be explained by other evolving structures along the line of sight. We define the full-width, half-maximum of the normalized Hi-C lightcurve at the center position of each loop (shown in the middle column) as the lifetime of the loop; the lifetimes are given in Table 1. The average lifetime is 64.0 s. We assume the error in the lifetime is the Hi-C image cadence, roughly 5.5 s.

Next we determine whether the loop appears simultaneously at all three position (east, center and west) or if the loop appears first at one location then later at another; perhaps caused by a flow of plasma from one footpoint to another or because of a temperature or density gradient along the loop. Loops A and F appear at all locations within two Hi-C images, meaning any apparent velocity cannot be measured with this cadence. The four remaining loops, however, do appear to demonstrate a delay between appearing at the eastern and western end. We determine the apparent velocity as the projected distance between the east
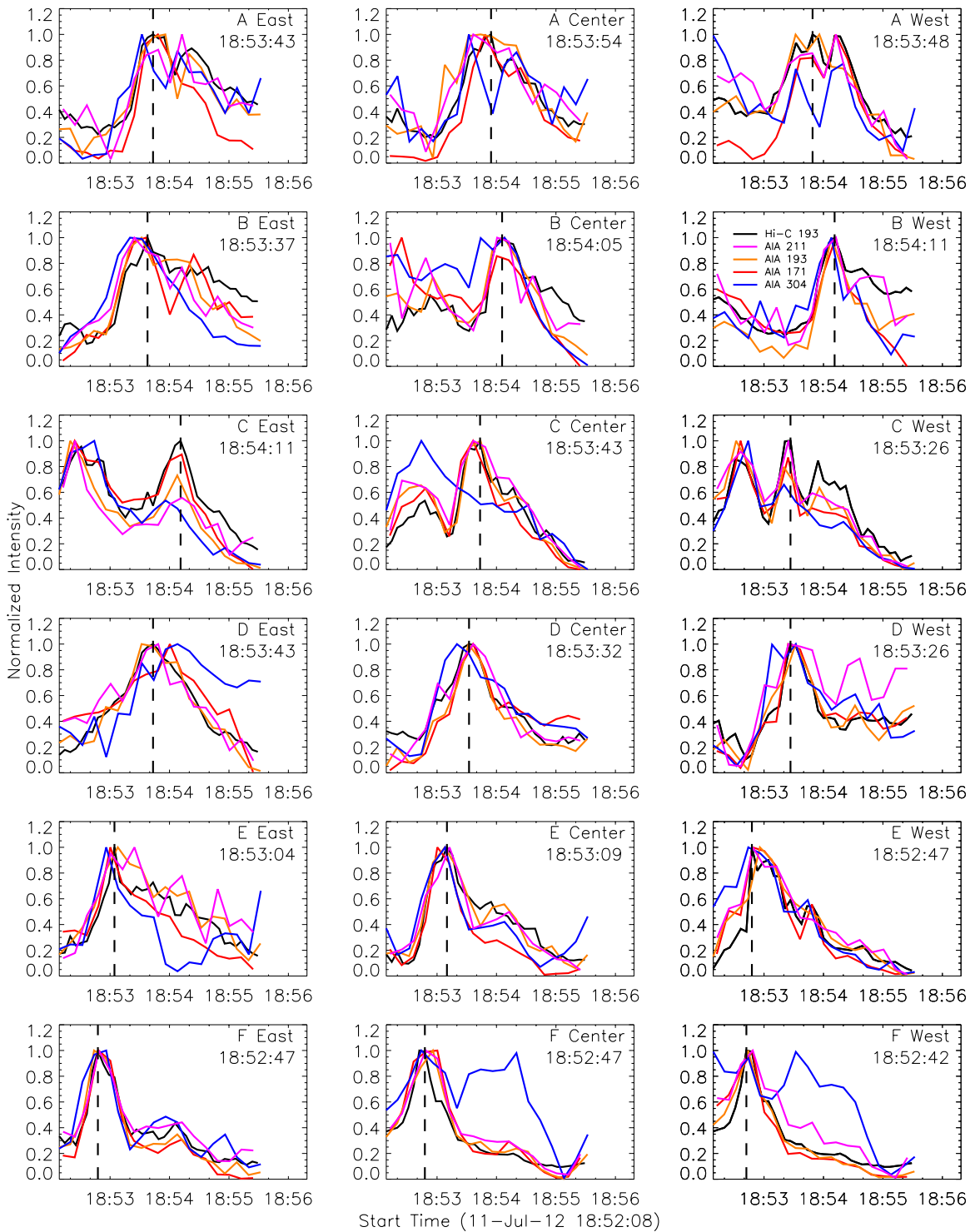
Figure 4. The lightcurves of the six loops measured at three locations along the loop in Hi-C and several AIA channels. The time where the Hi-C lightcurve peaks is shown with a vertical dashed line. The Hi-C 193 Å intensity is shown with a black line, the AIA 211, 193, 171, and 304 Å intensities are shown with purple, orange, red, and blue lines, respectively.

and west points (shown in Figure 2) divided by the difference in time of the peak of the Hi-C lightcurve at those two points. These velocities are given in Table 1. A positive velocity implies the loop appears at the east footpoint first, while negative values imply the loop appears at the west footpoint first. The apparent velocities range from 90 to 290 km s^{-1}.

Finally, we measure the projected length and diameter of the loop. To determine the projected length, we simply calculate

the total number of Hi-C pixels along the structure; multiply by the Hi-C resolution and the km per arcsec on 2012 July 11. The lengths are given in Table 1 and should be considered the lower limit to the true value due to both projection effects and the likelihood we are not observing the true footpoints of the loops.

To determine the diameter of the loop, we extract the intensity across the loop in Hi-C 193 Å passband from the center location
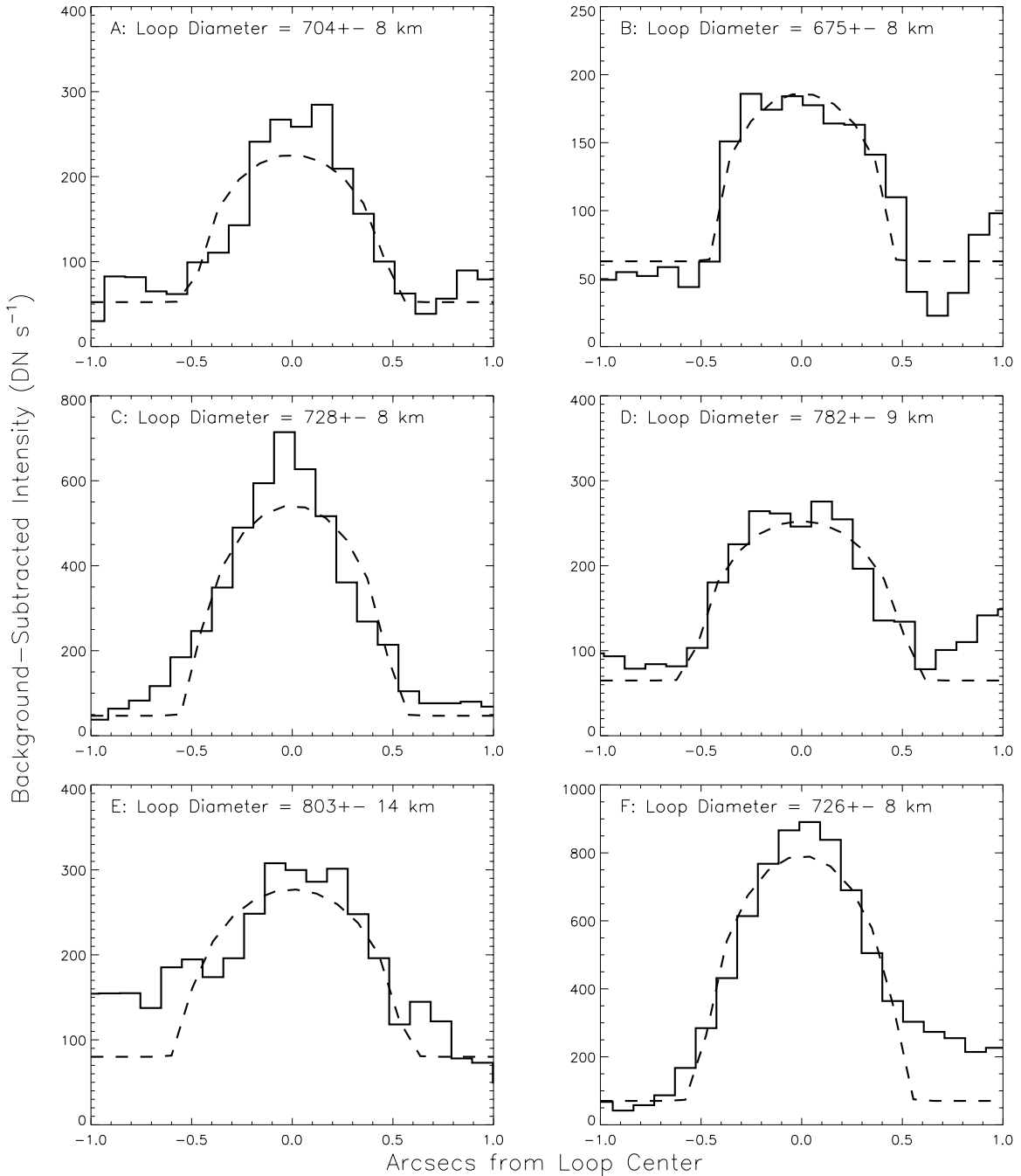
Figure 5. The Hi-C 193 Å intensity across the loops at their center position and the peak of the lightcurve (solid). The intensity profiles were fit assuming the emitting structure had a circular cross-section and the Hi-C point spread function was a Gaussian with a width of 0″.35. The diameter of the loop determined from the fit is given in each image and the fit is shown with a dashed line.

of each loop (shown in Figure 2 as a plus sign) and at the time of the peak in the lightcurve (shown in Figure 4 with a vertical dashed line). The intensities across the loop as a function of arcsecs are shown in Figure 5. Each intensity curve is fit with a function that assumes the emitting structure is cylindrical and the point spread function is Gaussian with a width of 0″.35. The fit is shown in Figure 5 with a dashed line. The resulting diameter of the cylinder is given in Figure 5 and in Table 1. The diameters of the loops range from 675 to 803 km.

2.2. Temperature, Emission Measure, and Density

When a structure is visible simultaneously in multiple AIA channels, it implies that the structure is either broadly multi-

thermal (i.e., formed of many smaller strands, each at a different temperature), or at a cool ($\sim 10^5$) temperature. (All AIA channels and the Hi-C channel have a cool-temperature response due to cool, relatively weak spectral lines present in the wavelength passband.) In the case of the loops analyzed in this paper, we also have the evolution of the loops in multiple channels to further discriminate between these two possibilities. These loops evolve roughly identically in all the AIA channels; such simultaneous evolution would be difficult to imagine if there are many sub-resolution strands at different temperatures, each evolving independently. Additionally, these loops are often bright in the 304 Å channel, and, in some cases, the 1600 Å channel, while being absent from the XRT Ti-poly and AIA
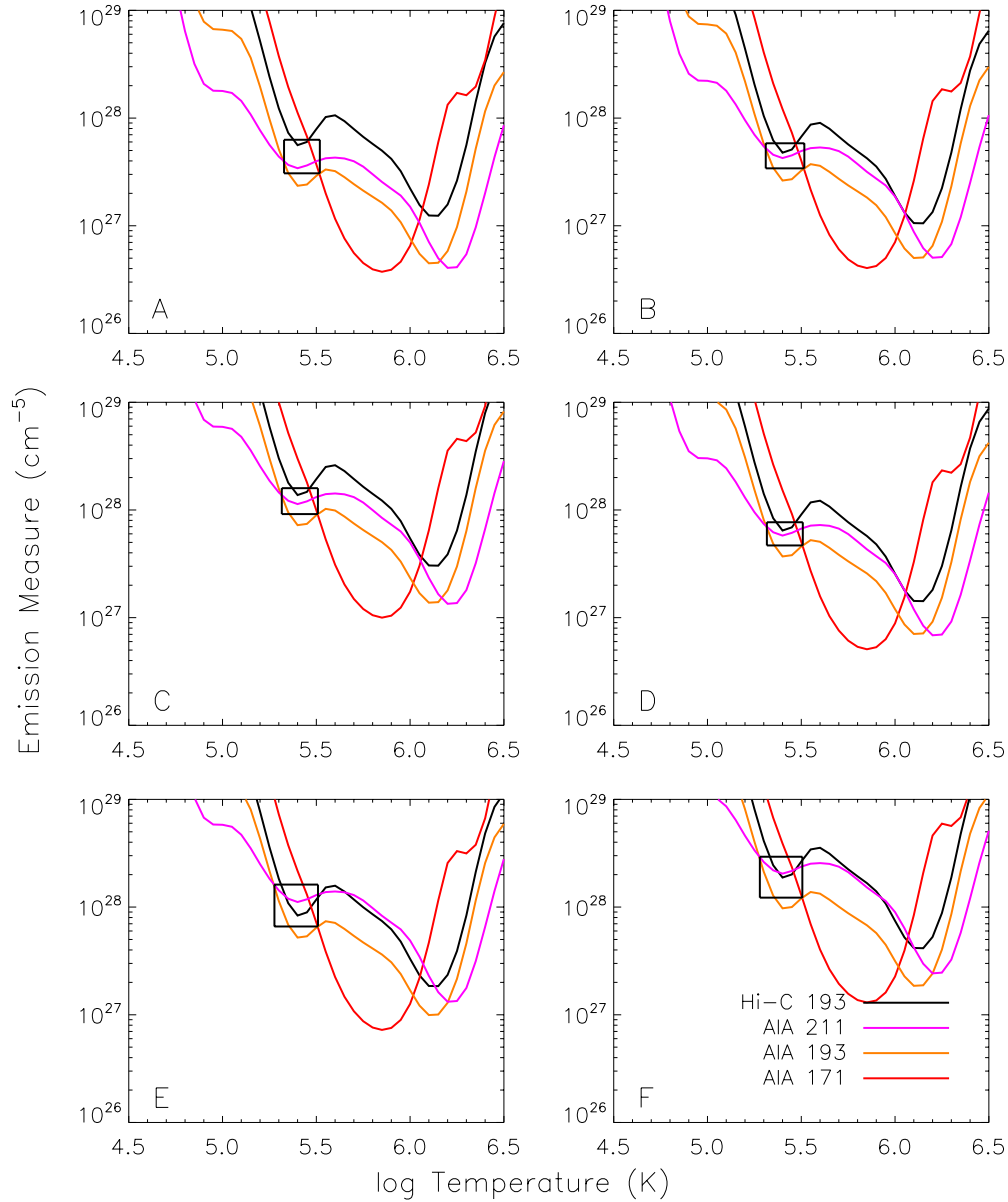
6

Figure 6. The EM Loci curves for the six loops. The curves show the intensity observed at the center position of each loop at the time of the peak Hi-C intensity divided by the response function for each channel. The black boxes show the range of temperatures and emission measures where the curves cross at a low temperature. The emission measure and temperature at the center of the box is given in Table 2. The error in these values is assumed to be half the dimension of the box. The Hi-C 193 Å curve is shown with a black line, the AIA 211, 193, and 171 Å curves are shown with purple, orange, and red lines, respectively.

94 Å images. These clues all indicate that the loops are likely cool structures.

Given that these are likely cool structures, it makes it difficult to determine their temperatures from the AIA temperature response curves using typical (i.e., differential emission measure) methods, as there is little temperature discrimination at the low temperatures in the AIA channels. Hence we use a simple EM Loci technique to determine a likely temperature and emission measure of these structures. We use the AIA 171, 193, and 211 Å channels and the Hi-C 193 Å channel. We first calculate the temperature response function of all channels assuming coronal abundances from Schmelz et al. (2012) and standard CHIANTI ionization equilibrium (Dere et al. 2009) and a constant pressure of 10^{16} K cm^{-3}. We then divide the background-subtracted intensity from the center pixel position at the time when Hi-C is at its peak by the response functions. Figure 6 shows the EM

Loci curves for the loops. The black boxes on each curve show the location of the crossings of the four curves at low temperatures. Table 2 gives the center position of the log temperature and emission measure shown in the black box with the error bars defined as the dimensions of the box. The most likely temperature in all cases is log $T \sim 5.4 \pm 0.1$ (i.e., 250,000 K). There are several potential sources of systematic error in both the temperature and emission measure estimate, including the uncertainty in the temperature response due to weak cool spectral lines in the AIA and Hi-C channels and the difference in spatial resolution between Hi-C and AIA.

Finally, we estimate the density of the loops by combining the emission measure in Table 2 with the loop diameter given in Table 1 and assuming a filling factor of 1. The density of each loop is given in Table 2. The densities of the loops are $\sim 10^{10}$ cm^{-3}.

Table 2
Loop Temperatures, Emission Measures, Densities, Radiated Energies, and Cooling Times

Loop	$\log T$	$\log$ EM	$\log n_e$	$\log$ Energy (erg)	Radiative Cooling Time (s)	Conductive Cooling Time (s)
A	5.42 ± 0.10	27.64 ± 0.16	9.94 ± 0.08	24.3	41.4	6.1×10^3
B	5.41 ± 0.10	27.65 ± 0.12	9.90 ± 0.06	24.6	43.5	1.3×10^4
C	5.41 ± 0.10	28.08 ± 0.12	10.11 ± 0.06	24.7	26.8	8.9×10^3
D	5.41 ± 0.10	27.78 ± 0.11	9.94 ± 0.06	24.7	39.7	9.7×10^3
E	5.39 ± 0.12	28.01 ± 0.19	10.06 ± 0.10	24.8	28.1	8.9×10^3
F	5.39 ± 0.11	28.28 ± 0.19	10.21 ± 0.10	24.8	19.9	1.2×10^4

3. DISCUSSION

In this paper, we have presented an analysis of six rapidly evolving loops observed during the Hi-C rocket flight. The high spatial resolution and cadence of the Hi-C data, combined with the multi-temperature coverage from the AIA data have allowed us to perform a detailed analysis of the loops properties. These are likely the smallest-scale EUV loops ever analyzed, with diameters of less than ~800 km and projected lengths less than 7.5 Mm. Using the Hi-C data, we estimate the apparent velocities along the loops; we find them to be >90 km s^{-1}. We see no indication that the loop plasma is cooling from million-degree temperatures. Instead, the evolution in the various AIA channels appears simultaneous, implying that the loops are isothermal and cool. We conclude that these inter-moss loops are likely composed of cool plasma and estimate a temperature of $10^{5.4}$ K and a density of 10^{10} cm^{-3}. This is not the first time that ~10^5 K plasma has been observed in an EUV channel thought to be dominated by million-degree plasma (see, e.g., Winebarger et al. 2002); the extent to which these cool plasma structures contribute to the emission in the EUV channels tuned to >10^6 K will be clarified with the upcoming launch of Interface Region Imaging Spectrograph (Wülser et al. 2013; De Pontieu et al. 2013).

We can use the analysis above to calculate the radiated energy of the loops,

$$E = n_e^2 P(T)\Delta t (\pi r^2) L, \qquad (1)$$

where n_e is the electron density from Table 2, $P(T)$ is the radiative loss function in erg cm^3 s^{-1} for the coronal abundances (Schmelz et al. 2012) and the standard CHIANTI ionization equilibrium (Dere et al. 2009), Δt is the lifetime, r is the radius, and L is the projected length of the loop from Table 1. The resulting energy in erg is given in Table 2. The fact that the structures are short lived imply they are heated impulsively; the energy range falls in that of "nanoflares," estimated to be 10^{24} erg by Parker (1988).

We can additionally calculate the radiative cooling time of these loops (e.g., Cargill & Klimchuk 1997, 2004) using

$$\tau_R = \frac{3k_B T}{n P(T)}, \qquad (2)$$

where k_B is Boltzmann's constant. The radiative cooling times are also given in Table 2. The cooling times are on the order of tens of seconds and are consistent with the observed lifetimes of the loops. We note that, for these loops, the conductive cooling time,

$$\tau_C = 4 \times 10^{-10} \frac{nL^2}{T^{5/2}} \mathrm{s}, \qquad (3)$$

where L is the loop half-length in centimeters, is much longer than the radiative cooling time (see Table 2).

Further confirmation of the nature of these loops and more detailed insight into their temporal evolution comes from a comparison with three-dimensional radiative MHD simulations of the solar atmosphere. These simulations, completed with a hypothetical magnetic field configuration, show very similar highly dynamic loop-like features that occur as a result of rapid heating from magnetic energy release at low heights and subsequent radiative cooling of the dense loop plasma.

These "realistic" three-dimensional simulations cover a numerical domain that spans from the convection zone to the corona and are based on the Bifrost code (e.g., Gudiksen et al. 2011; Hansteen et al. 2007, 2010). In these simulations a convective photospheric model with an effective temperature $T_{\mathrm{eff}} = 5780$ K is extended into the chromosphere and lower corona. The model has 24×24 Mm^2 horizontal dimensions, extends 2.5 Mm below the photosphere and 14 Mm above. A largely bipolar potential magnetic field with poles some 8 Mm apart is inserted into the model and is thereafter subjected to convective motions. The heating of the outer atmospheric regions is ensured by the inclusion of this magnetic field, which is stressed by the convective motions of the photosphere and below. This stressing gives rise to field aligned currents and Joule heating. The mean distance between opposite magnetic polarities sets the scale height of the magnetic field. In the model described the typical distance between polarities ranges from granular up to the scale of the originally inserted magnetic field. This means that we find many loops with an apex near the top of the chromosphere and bottom of the corona, i.e., some 2–3 Mm above the photosphere. In this magnetic field configuration such low-lying loops occur much more frequently than those that extend high into the corona.

Given their low apex heights, these loops are of rather high density. Since radiative losses scale with the density squared, the loops cool efficiently making it difficult for these loops to reach coronal temperatures. When subjected to highly episodic Joule heating, these loops thus tend to cycle between chromospheric and lower transition region temperatures. In Figure 7 we show the emission from the transition region Si IV 1393 Å spectral line ($\log T = 4.8$) as seen from the side and from above. The magnetic field lines of a low lying loop, from photosphere to apex, are overplotted as a function of time at 10 s intervals for a duration of 150 s. In Figure 8 we show the time evolution of the temperature and density in this loop: episodic heating raises the temperature along a 4 Mm long stretch, from 50 kK up to 600 kK and back down to lower transition temperatures during a period of 150 s. The density in the heated region of the loops varies between 3×10^9 cm^{-3} and 10^{10} cm^{-3} in the same time span. As illustrated by Figure 7 we find many examples of this kind of low lying cool loop in the simulations.

The high densities, low temperatures and short lifetimes show a remarkable correspondence with our Hi-C observations. Our simulations show that such loops occur naturally as a result of
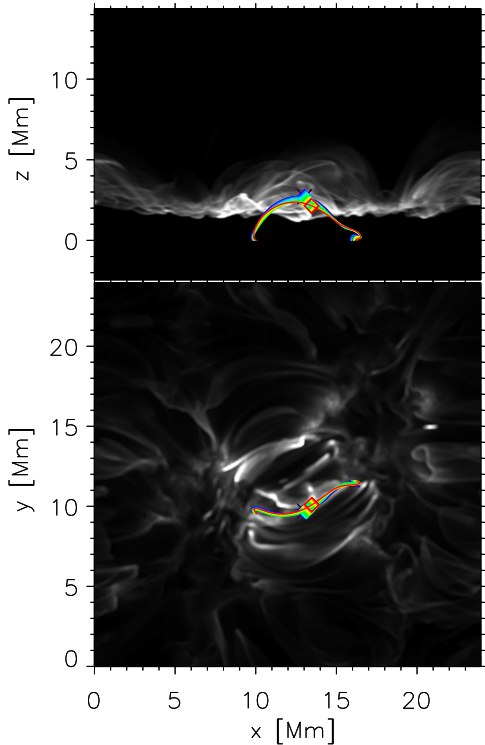
Figure 7. Total simulated intensity in the lower transition region Si IV 1393 Å emission line as seen from the side and from above. Overplotted are the magnetic field lines of a typical low lying transition region temperature loop that is heated from, and cools to, chromospheric temperatures during a period of 150 s. The field lines are plotted at intervals of 10 s, starting at black, through blue, green, yellow, to red after 150 s.

Figure 8. Simulated temperature (top panel) and number density along the field lines plotted in Figure 7. The field lines are followed from photospheric footpoint ($z = 0$ Mm) to photospheric footpoint. The field lines are plotted at intervals of 10 s, starting at black, through blue, green, yellow, to red after 150 s.

rapid magnetic energy release (in this case from reconnection of braided magnetic field lines) at chromospheric/low coronal heights in low-lying loops. Such loops tend to occur in a magnetic field configuration where footpoints are separated by only a few Mm (as in our observations) so that the loop apex is only a few Mm above the photosphere. All of these conditions appear to be fulfilled in the loops we study in our Hi-C observations. The rapid temporal evolution occurs naturally from a combination of short-term heating ("nanoflare") and rapid radiative cooling in the dense, low-lying plasma in these short loops. Synthetic images of low transition region lines from the simulations show evidence of very high apparent velocities, similar to those observed with Hi-C. These high apparent velocities in the simulations are not caused by plasma flows, but rather occur because of the rapid thermal conduction.

Our simulations thus strongly support our interpretation of these cool, dense and dynamic transition region loops being caused by nanoflares at low heights and subsequent rapid radiative cooling. More extensive high resolution observations (similar to these Hi-C measurements) combined with advanced numerical simulations will be required to determine how prevalent these loops are and what role they play in the energy balance of the solar atmosphere.

Though we have discovered and characterized these subarcsecond inter-moss transition region loops, we have not found evidence of inter-moss coronal loops cooling from millions of degrees as predicted by the long nanoflare storm heating scenario of Klimchuk (2006). With Hi-C's spatial resolution and cadence, it seems likely that these expected cooling core loops would have been observed by Hi-C if they were present. Their lack of detection implies either that hardly any high-temperature
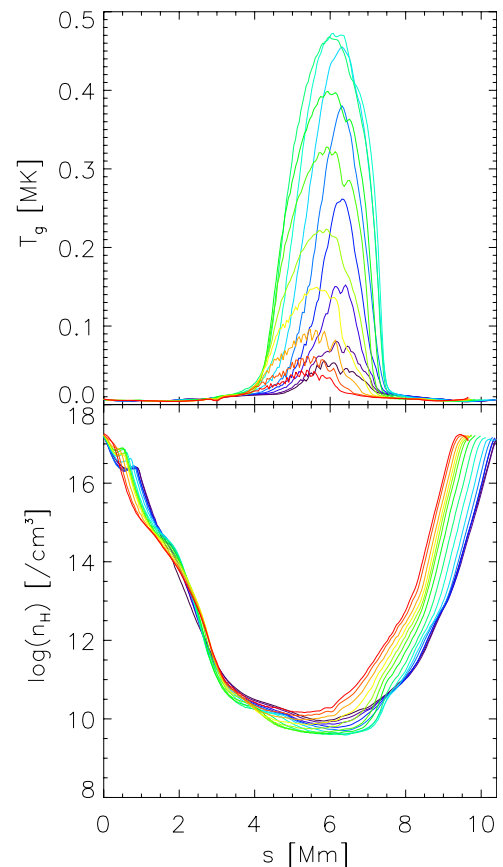
inter-moss coronal loops cool through 1 MK to lower temperatures (i.e., that the heating events are at a high-enough sustained frequency to maintain these loops at temperatures above 1 MK) or that any cooled strands are so far below the resolution of Hi-C that they are too faint to be detected in the Hi-C images.

REFERENCES

Antiochos, S. K., Karpen, J. T., DeLuca, E. E., Golub, L., & Hamilton, P. 2003, ApJ, 590, 547
Aschwanden, M. J., Tarbell, T. D., Nightingale, R. W., et al. 2000, ApJ, 535, 1047
Berger, T. E., De Pontieu, B., Fletcher, L., et al. 1999, SoPh, 190, 409
Bradshaw, S. J., Klimchuk, J. A., & Reep, J. W. 2012, ApJ, 758, 53
Cargill, P. J., & Klimchuk, J. A. 1997, ApJ, 478, 799
Cargill, P. J., & Klimchuk, J. A. 2004, ApJ, 605, 911
Cirtain, J. W., Golub, L., Winebarger, A. R., et al. 2013, Natur, 493, 501
De Pontieu, B., Berger, T. E., Schrijver, C. J., & Title, A. M. 1999, SoPh, 190, 419
De Pontieu, B., et al. 2013, SoPh, in press
Dere, K. P., Landi, E., Young, P. R., et al. 2009, A&A, 498, 915
Fletcher, L., & de Pontieu, B. 1999, ApJL, 520, L135

Golub, L., Deluca, E., Austin, G., et al. 2007, SoPh, 243, 63

Gudiksen, B. V., Carlsson, M., Hansteen, V. H., et al. 2011, A&A, 531, A154

Hansteen, V. H., Carlsson, M., & Gudiksen, B. 2007, in ASP Conf. Ser. 368, The Physics of Chromospheric Plasmas, ed. P. Heinzel, I. Dorotovič, & R. J. Rutten (San Francisco, CA: ASP), 107

Hansteen, V. H., Hara, H., De Pontieu, B., & Carlsson, M. 2010, ApJ, 718, 1070

Klimchuk, J. A. 2006, SoPh, 234, 41

Klimchuk, J. A. 2009, in ASP Conf. Ser. 415, ed. B. Lites, M. Cheung, T. Magara, J. Mariska, & K. Reeves (San Francisco, CA: ASP), 221

Kobayashi, K., et al. 2013, SoPh, in press

Lemen, J. R., Title, A. M., Akin, D. J., et al. 2012, SoPh, 275, 17

Lenz, D. D., Deluca, E. E., Golub, L., Rosner, R., & Bookbinder, J. A. 1999a, ApJL, 517, L155

Lenz, D. D., DeLuca, E. E., Golub, L., et al. 1999b, SoPh, 190, 131

Mulu-Moore, F. M., Winebarger, A. R., Warren, H. P., & Aschwanden, M. J. 2011, ApJ, 733, 59

Parker, E. N. 1988, ApJ, 330, 474

Patsourakos, S., & Klimchuk, J. A. 2005, ApJ, 628, 1023

Reale, F. 2010, LRSP, 7, 5

Sarkar, A., & Walsh, R. W. 2008, ApJ, 683, 516

Sarkar, A., & Walsh, R. W. 2009, ApJ, 699, 1480

Schmelz, J. T., Reames, D. V., von Steiger, R., & Basu, S. 2012, ApJ, 755, 33

Viall, N. M., & Klimchuk, J. A. 2012, ApJ, 753, 35

Warren, H. P., Brooks, D. H., & Winebarger, A. R. 2011, ApJ, 734, 90

Warren, H. P., Winebarger, A. R., & Brooks, D. H. 2010, ApJ, 711, 228

Warren, H. P., Winebarger, A. R., & Hamilton, P. S. 2002, ApJL, 579, L41

Warren, H. P., Winebarger, A. R., & Mariska, J. T. 2003, ApJ, 593, 1174

Winebarger, A. R., Updike, A. C., & Reeves, K. K. 2002, ApJL, 570, L105

Winebarger, A. R., Warren, H. P., & Mariska, J. T. 2003, ApJ, 587, 439

Winebarger, A. R., Warren, H. P., & Seaton, D. B. 2003, ApJ, 593, 1164

Wülser, J.-P., Title, A. M., Lemen, J. R., et al. 2012, Proc. SPIE, 8443, 844308